PAPER

One-pot green synthesis of rGO/SnO$_2$ nanocomposites from cellulose and SnCl$_2$ as Lewis acid catalyst

Loubna Jabir, [ID] *[a] Omar Azougagh, [ID] [a] Hicham Ait Laasri,[b] Nor Mohammed,[c] Issam Jilal,[d] Youssef El Ouardi,[e] Damien Brault,[b] Hayat El-Hammi,[a] M'hamed Ahari,[c] Amine Salhi, [ID] [c] Mohamed Abou-Salama, [ID] [a] Mustapha Zaghrioui,[b] Elkhadir Gharibi [ID] *[f] and Soufian El Barkany*[a]

The development of sustainable, single-step protocols for fabricating metal oxide-graphene heterostructures remains a critical challenge to overcome the toxicity and complexity of conventional synthesis methods. In this regard, this paper reports a one-pot, cellulose-based hydrothermal route for obtaining reduced graphene oxide/tin dioxide (rGO/SnO$_2$) nanocomposites. This route exploits tin(II) chloride as a dual-action reducing agent (Lewis acid) and isomerization/dehydration catalyst, inducing the cellulose → glucose → fructose → 5-HMF reaction cascade and the concomitant aromatization to sp^2 carbon while oxidizing Sn^{2+} to rutile SnO$_2$. The process yields uniformly dispersed SnO$_2$ nanocrystallites anchored on few-layer reduced graphene, as confirmed by ATR-FTIR/Raman, XRD, SEM/EDX, and TEM. Raman analysis shows low structural disorder (D/G $\approx$ 1.72), XRD identifies rutile SnO$_2$ with an average crystallite size of $\sim$5.4 nm, and TEM reveals a homogeneous nano-SnO$_2$ distribution on wrinkled rGO sheets. TGA indicates a Csp^2/SnO$_2$ mass ratio of $\sim$8, supporting high graphitic content. Density functional theory on a representative Sn$_3$O$_6$-rGO model indicates a moderate HOMO–LUMO gap ($\sim$1.30 eV), substantial electrophilicity, and a balanced electrostatic potential, consistent with efficient interfacial electronic communication and adsorption-driven reactivity. By integrating *in situ* nucleation of ultrasmall SnO$_2$ with the formation of conductive rGO, the architecture aligns with state-of-the-art SnO$_2$/graphene hybrids known to accelerate charge transport and redox kinetics for energy storage, catalysis, and gas sensing. The green, single-step workflow avoids external reducing agents and graphitic exfoliation steps, offering a scalable pathway to high-quality SnO$_2$/rGO heterointerfaces that are broadly applicable to electrochemical, photocatalytic, and room-temperature sensing platforms.

1 Introduction

Tin dioxide and graphene derivative nanocomposites (SnO$_2$/GO and SnO$_2$/rGO) have garnered significant interest due to their synergistic electrical, optical, catalytic, electrochemical, and dielectric properties.[1] These hybrids are model platforms where intimate SnO$_2$-graphitic interfaces enhance redox kinetics, electron percolation, and charge separation while suppressing carrier recombination.[2,3] This underpins state-of-the-art performance in energy storage for alkali-ion batteries,[4] electrocatalysis such as nitrogen reduction[5] and oxygen reduction in microbial fuel cells,[6] and photocatalysis for degrading organic dyes.[7,8] The design of such multiphase hybrids relies heavily on optimizing the heterojunction to facilitate charge transfer, a concept extensively explored in recent literature regarding doping and nanocomposite engineering.[9,10] Furthermore, their potential in optical and semiconductor applications[11] and high-performance room-temperature gas sensing, achieved through optimized microstructures and p–n junction effects,[12,13] is well-established.

Despite these advances, the sustainable synthesis of high-quality graphitic composites remains a challenge. Moreover, several research efforts have contributed to the development of alternative graphitic materials meeting the desired

[a]*Laboratory of Molecular Chemistry, Materials and Environment (LMCME), Department of Chemistry, Faculty Multidisciplinary Nador, Mohamed, 1st University, P. B. 300, Nador 62,700, Morocco. E-mail: el.barkany011@gmail.com; ja.loubna@gmail.com*

[b]*GREMAN, Université de Tours – CNRS – INSA Centre Val de Loire – UMR7347, IUT de Blois, 15 Rue de la Chocolaterie, CS 32903, 41029 Blois Cedex, France*

[c]*Applied Chemistry Unit, Sciences and Technologies Faculty, Abdelmalek Essaadi University, 32 003 Al Hoceima, Morocco*

[d]*LIMOME Laboratory, Sidi Mohamed Ben Abdallah University, Faculty of Sciences Dhar El Mehraz, Dhar El Mehraz B.P. 1796 Atlas, Fes 30000, Morocco*

[e]*Laboratory of Separation Technology, Lappeenranta University of Technology, P. O. Box 20, FI-53851 Lappeenranta, Finland*

[f]*Laboratory of Applied Chemistry and Environmental (LCAE-URAC18), Faculty of Sciences of Oujda, Morocco. E-mail: gharibi_elkhadir@yahoo.fr*

characteristics,[14] including increasing the reduction rate of GO, which could improve its structural, optical, magnetic, and electrical properties.[15,16] The electrochemical route for GO reduction is the predominant route in almost all published works, using several popular types of reducing agents, such as strong alkaline hydrazine,[17] hydroquinone,[18] sodium borohydride,[19] hydrohalic acids[20] and green agents such as ascorbic acid,[21,22] ethylene glycol,[23] glucose[24] and vitamin C (ref. 25) that have been proposed. The methods generally still require a pre-exfoliation step of graphite. This exfoliation is essential to increase the accessibility of tin ions involved in the subsequent reaction for the reduction of the exfoliated graphite,[26,27] yet physical and chemical exfoliation often produces a heterogeneous variety of nitrogenous or oxygenated graphene-based sheets, such as reduced graphene oxide (rGO).[28] In addition, the rGO possesses more active sites with an enlarged interlayer distance, despite the high temperature operating (2500 °C).[29]

However, this approach is hindered by the heterogeneous distribution of oxygenated zones on the carbon surface, which promotes stannic agglomeration and results in poor interfacial contact.[30] This contact heterogeneity at the supramolecular scale introduces structural defects, thereby limiting the application of these composites in high-precision electronic devices, particularly those involving chemical vapor deposition (CVD)[30] and epitaxial growth methods.[31]

Various techniques have been employed to introduce SnO_2 into the carbon matrix, including spray drying,[32] microwave,[33] ultrasonic treatment[34] and hydrothermal[35] methods. Among these, the hydrothermal technique is often preferred due to its ability to yield desired sheet morphologies and tuned hybrid nanostructure dimensions.[35] The hydrothermal method is recognized as the most direct and simplest pathway for the *in situ* incorporation of metal oxides within graphene nanosheets,[36] offering advantages such as relatively low temperatures, simple equipment, low costs, and high efficiency.[37] Furthermore, it offers distinct advantages in controlling porosity and crystallite size compared to precipitation or sol–gel methods.[10,38–40] Despite the versatility of hydrothermal synthesis, conventional pathways remain fundamentally multistep, often rely on toxic chemicals, and start from processed graphite or graphene oxide. Consequently, a significant gap exists in the development of a truly green, one-pot hydrothermal synthesis that starts directly from a raw, renewable carbon source. Such an approach would simultaneously form the rGO matrix and SnO_2 nanoparticles *in situ*, ensuring homogeneous integration and overcoming the need for separate exfoliation, reduction, and composite formation steps.

In this work, we present a new eco-friendly and sustainable approach for the production of homogeneous rGO/SnO_2 nanocomposites that avoids the agglomeration issues inherent in multi-step mixing and minimizes the use of harsh chemicals. Unlike conventional methods that require pre-synthesized graphene oxide or toxic reducing agents, this work establishes a singular $SnCl_2$-mediated pathway. This significantly lowers the *E*-factor of the process while ensuring intimate interfacial contact between the *in situ* formed SnO_2 and the rGO matrix. We utilize native cellulose as a renewable carbon source and tin(II)

chloride Lewis acid as a bifunctional catalyst/precursor. Cellulose is the most abundant bioresource and exhibits excellent macromolecular properties.[41–44] This one-pot hydrothermal synthesis drives the simultaneous carbonization of cellulose and nucleation of SnO_2, validated by recent advances in biomass-derived carbon materials.[45] The electronic properties of the resulting nanocomposites were further investigated using computational calculations based on density functional theory (DFT),[46] providing relevant information on the electronic structure and potential applications of the material.

2 Materials and methods

2.1 Materials

Cellulose powder (M_w ~35.5 10^3 Da) and tin(II) chloride dihydrate ($SnCl_2 \cdot 2H_2O$) were purchased from Sigma-Aldrich Company. The deionized water used for the preparation of aqueous solutions was obtained from the Milli-Q® System. For comparative characterization, pure tin(IV) oxide (SnO_2) nanopowder, ≤100 nm avg. part. size, was obtained from Sigma-Aldrich. All chemicals are of analytical grade and were used as received without any further purification.

2.2 Methods

The vibrational ATR-FTIR spectra was investigated to evaluate the proposed nanocomposite chemical structure and were recorded on JASCOFT/IR-4700-ATR Spectrometer (40 scans, 4000–400 cm^{-1}). The X-ray diffraction patterns were recorded using D8 Focus X-ray diffractometer (Bruker equipment), applying CuK$_\alpha$ ($\lambda = 1.5418$ Å), at 40 kV and 30 mA as accelerating voltage and operating current, respectively. All patterns were registered in the range of 2θ (10°–80°) and the scan rate was set to 3 min. Thermal stability SnO_2/rGO nanocomposite (8–12 mg) were studied basing on thermogravimetric analysis (TGA/DrTGA) recorded on a Shimadzu DTG-60 simultaneous DTA-TG apparatus. Two scans were run from room temperature to 900 °C at a rate of 10 °C min^{-1} under N_2 flow. The morphology changes and microstructural profile were examined using *MIRA 3 SEM* Scanning Electron Microscopy (SEM) *TESCAN VEGA 3 LM* microscope, where secondary electrons were analyzed at an acceleration voltage of 5 kV. The elemental surface profile was studied using Energy-Dispersive X-ray (EDX) spectroscopy coupled to the electron scanning microscopy imaging. Raman spectra of rGO/SnO_2 nanocomposite were recorded on RENISHAW InVIA Reflex Raman spectrometer, equipped with Edge-filter, and the excitation was carried out using the argon ion laser polarized radiation ($\lambda = 633$ nm). For TEM imaging, the samples were characterized using a *Hitachi HT7700* transmission electron microscope.

2.3 Preparation of SnO_2/rGO nanocomposite and pure SnO_2

1.7 g (10.5 mmol) of cellulose and 2.366 g (10.5 mmol) $SnCl_2$, $2H_2O$ were dispersed in a 50 ml Teflon beaker containing 17 ml of deionized water. The dispersion was stirred for 20 min, then transferred into a Teflon-lined autoclave and hydrothermally treated at 200 °C for 8 h. After cooling, the resulting brown

mixture was centrifuged at 9000 rpm for 30 minutes. The solid product was collected by vacuum filtration, rinsed thoroughly with deionized water, dried in an oven at 105 °C for 24 h, and finally desiccated under vacuum over phosphorus pentoxide (P_2O_5) for one week.

3 Results and discussions

3.1 One-pot cellulose-based synthesis of SnO_2/rGO nanocomposite

The proposed mechanism of the hydrothermal synthesis of cellulose-based reduced graphene oxide (rGO)/SnO_2 nanocomposite is shown in Fig. 1. Tin(II) chloride Lewis acid showed a drastic effect as reducer and isomerization/dehydration catalyst (glucose → fructose → 5-HMF),[47,48] where no reaction was observed in the absence of stannous ions, except for a slight increase in cellulose crystallinity which is due to the degradation of the small fraction of amorphous polymer. However, the resulting reduced graphene oxygen (rGO) with SnO_2 has been investigated. Indeed, water produces large amounts of H^+ and OH^- under hydrothermal conditions (at high temperature and pressure), then the cellulose hydrolysis proceeds successively under the action of H^+ and OH^- ions, which causes the formation of a variety of components such as glucose, cellobiose, levoglucosan and clusters of crystalline cellulose. As the hydrolysis reaction progressed, the yield of glucose became higher and higher, and glucose became the main product. Under the catalytic effect of $SnCl_2$, the isomerization/ dehydration of glucose to fructose and then to 5-HMF allows the Sp^2 carbon polymerization under hydrothermal conditions. On the other hand, the oxidation of stannous ions (Sn^{2+}/Sn^{4+}) generates the "*in situ*" formation of tin oxide nanoparticles (SnO_2) in parallel with the polymerization and aromatization of 5-HMF, followed by intermolecular condensation to form the sp^2 aromatic carbon network, which condenses to form the final product (Fig. 1).

3.2 Spectral and structural analysis

3.2.1 Thermogravimetric analysis (TGA-drTGA). The thermal stability of the rGO/SnO_2 nanocomposite was evaluated by thermogravimetric analysis (TGA) and its derivative (DTG), as presented in Fig. 2. The initial endothermic mass loss, observed from ambient temperature to approximately 100 °C, is attributed to the evaporation of physisorbed water. A subsequent major exothermic mass loss event occurring between 250 and 550 °C is associated with the thermal decomposition of oxygen-containing functional groups and the combustion of the reduced graphene oxide carbon skeleton.[49] The overall mass loss for the rGO/SnO_2 composite over this temperature range (RT to 550 °C) was measured to be 40%. This significant mass loss indicates a high carbon-to-metal oxide ratio within the composite, suggesting an extensive C=C sp^2 carbon network relative to the SnO_2 content.[50]

3.2.2 Fourier transform infrared (ATR-FTIR). The ATR-FTIR spectra of native cellulose and rGO/SnO_2 nanocomposite are shown in Fig. 3. The native cellulose spectrum reveals all the typical characteristic absorption bands of cellulose structure around 3420, 2940, 1647, 1440, 1388, 1335, 1262, 1169, 1073 and 903 cm^{-1}. The broad band at 3420 cm^{-1} is attributed to the O–H stretching vibration, and the absorption band located at 2940 cm^{-1} is linked to the C–H stretching vibration.[51,52] Also, the absorption bands detected at 1440 and 1388 cm^{-1} are associated to the planar deformation of primary alcohol (O–H) and the C–H bending vibration in –CH–OH, respectively.[53] Whereas the band at 1647 cm^{-1} correspond to H_2O naturally absorbed within the cellulosic structure.[54] Furthermore, the absorption bands detected at 1335 cm^{-1} and 1262 cm^{-1} are associated to the typical C–C and C–O vibrations of the cellulosic backbone.[55] In addition, the absorption bands at 1169 cm^{-1} and 1073 cm^{-1} approved the asymmetric C–O vibration and the stretching C–O–C vibration of the glucopyranose skeleton, respectively.[56] The band at 903 cm^{-1} is a characteristic of the β-(1,4) glycoside bond.[57] However, the rGO/SnO_2 nanocomposite spectrum showed the appearance of new absorption band at 1625 cm^{-1} attributed to the sp^2 C=C aromatic vibrations,[58-60] indicating that the synthesis of graphene plan structure from native cellulose was carried out successfully. In addition, the new band detected at 1703 cm^{-1} is assigned to the stretching vibrations of the C=O carboxylic carbonyl.[61,62] While, the absorption band recorded at 1244 cm^{-1} is originated from (C–O) epoxy.[60] Moreover, the characteristic bands situated around 3421 cm^{-1} and 2920 cm^{-1} are attributed to the O–H stretching vibration and sp^3 CH_2 stretching vibration, respectively.[63,64] It is also observed that in the nanocomposite, the SnO_2 bands at 524 cm^{-1} and 663 cm^{-1} are assigned to the stretching Sn–O–Sn and stretching modes Sn–O, respectively.[65] The ATR-FTIR results exhibit the success of the formation of SnO_2 nanoparticles within reduced graphene oxide nanosheets in single and continuous structure rGO/SnO_2 as supported by the XRD data.

3.2.3 Raman scattering analysis. Raman spectroscopy (Fig. 4) reveals two characteristic peaks at 1381 cm^{-1} (D band) and 1594 cm^{-1} (G band). The D band is associated with defects and disorder, while the G band arises from the in-plane vibration of sp^2 carbon atoms. The presence of the G band confirms the formation of a graphitic structure.[66] The peak located at 631 cm^{-1} is assigned to A_{1g} vibration mode of SnO_2.

Comparison with literature values for standard reduced graphene oxide typically shows a D band near 1350 cm^{-1} and a G band near 1580 cm^{-1}. The observed shift to 1381 cm^{-1} and 1594 cm^{-1} in our composite indicates a strong electronic interaction between the SnO_2 nanoparticles and the carbon matrix, as well as lattice strain induced by the anchoring of the oxides.[67] However, the slight shift of the G-light scattering peak confirmed the predominance of the C=C structural profile of graphene. The D-band is associated with the defect states in the graphene structure, where the intensity of the D-band is affected by the defect density and the existence of oxygen atoms on the rGO surface.[68] The appearance of the G band in the SnO_2/rGO nanocomposite structure confirms the formation of the sp^2 (C=C) carbon–carbon bonds characteristic of graphene planes, and therefore constitutes a strong indication that the synthesis of the graphene structure from native cellulose has been
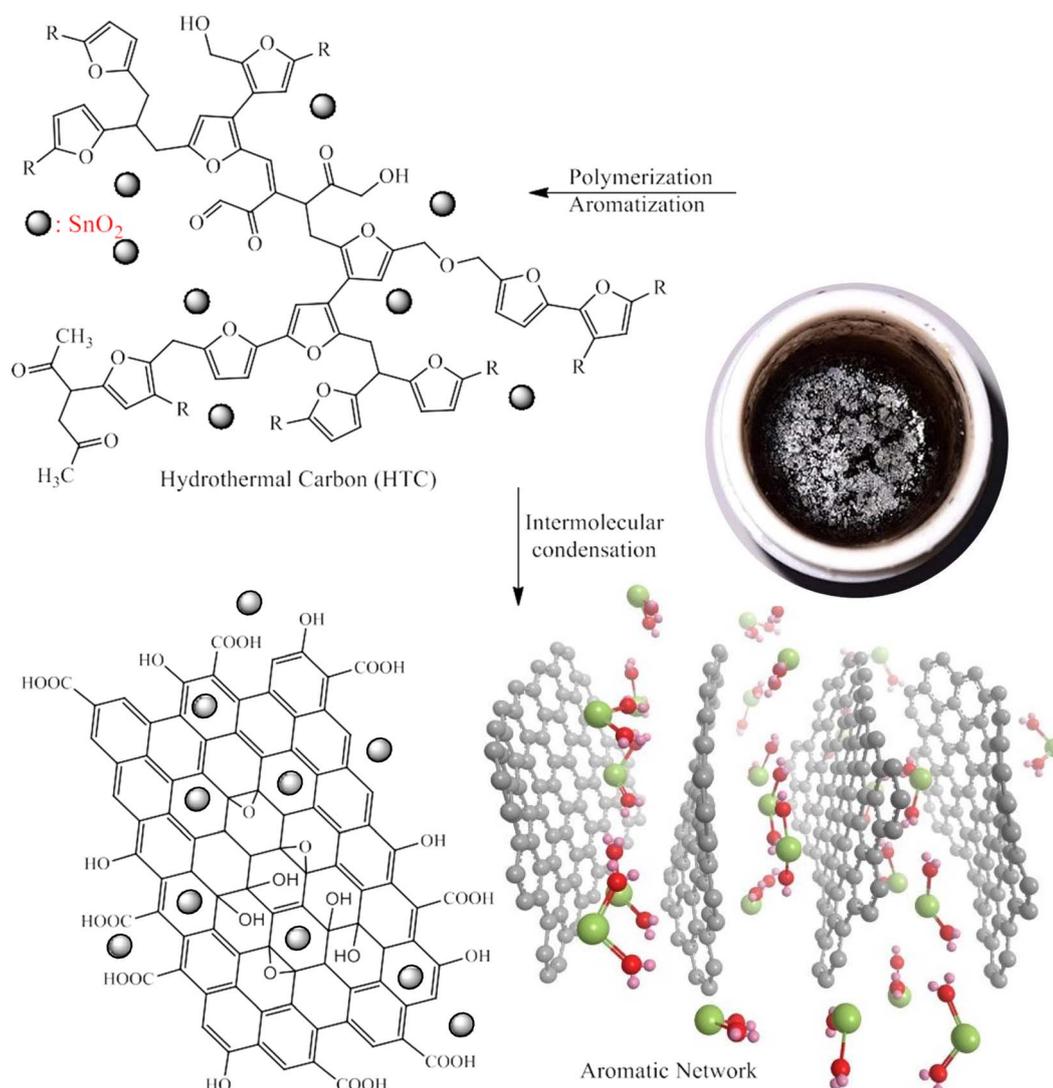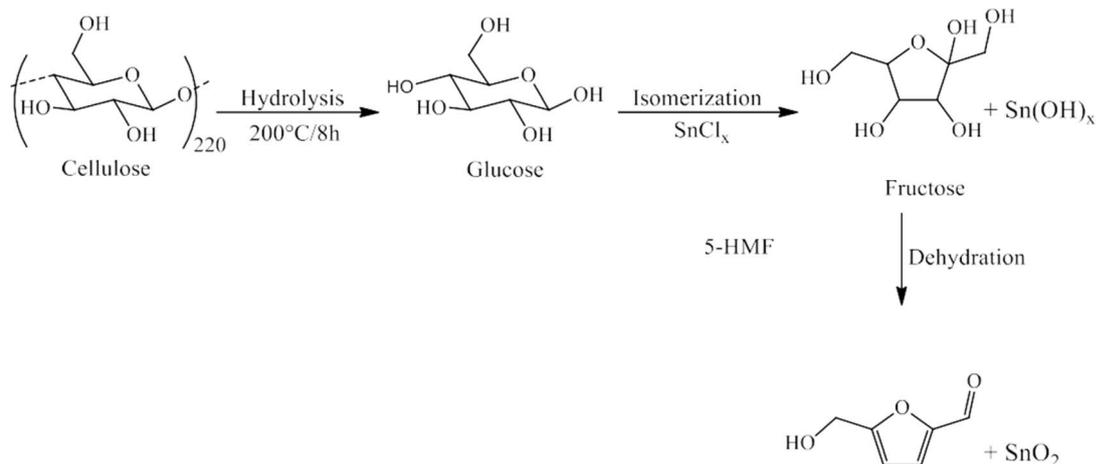
Fig. 1 Synthesis route of rGO/SnO$_2$ nanocomposite from cellulose and SnCl$_2$ as Lewis acid catalyst (cellulose → glucose → 5-HMF → rGO/SnO$_2$).

successfully achieved.[69] Thus, the degree of disorder and the length of defects (heteroatom/vacancy or C–Csp^3) can be evaluated using the intensities of different Raman scattering peaks.

In this paper, the intensities of the D and G peaks were used to evaluate the level of disorder in the SnO$_2$/rGO nanocomposite. In this regard, the ratio of D/G peak's areas reflects two distinct
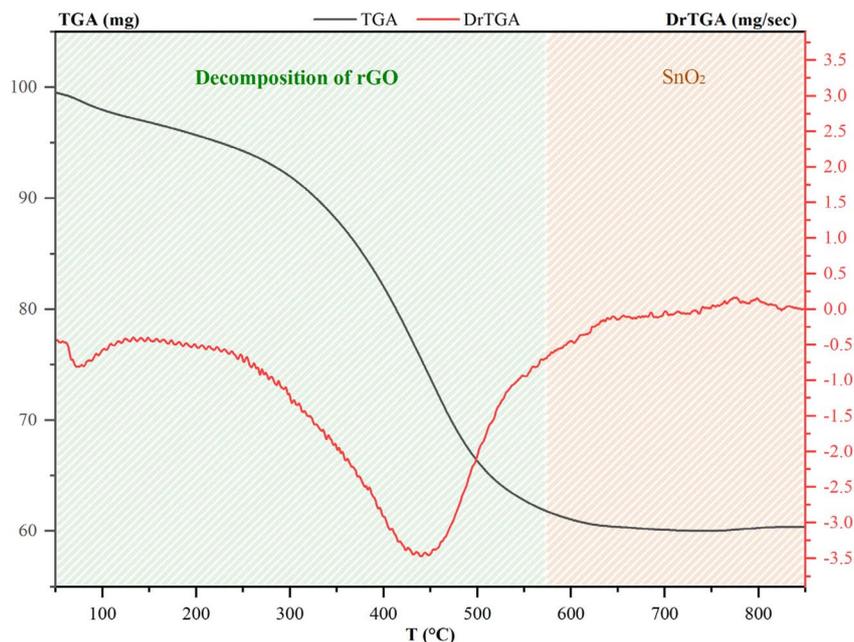
Fig. 2 TGA-DrTGA thermograms of rGO/SnO$_2$ nanocomposite.
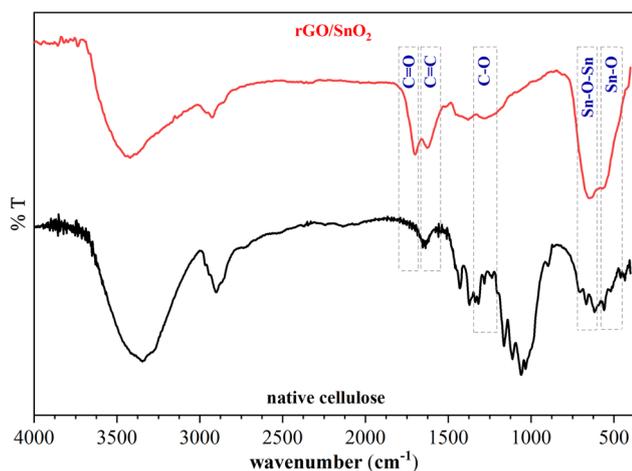
Fig. 3 FTIR-ATR spectra of native cellulose (a) and rGO/SnO$_2$ nano-composites (b).

behaviors depending on the disorder density in the graphene material. The I_D/I_G ratio is approximately 1.72. While this indicates a degree of disorder typical for hydrothermal carbons, it is significantly lower than amorphous carbons (I_D/I_G >3.5), suggesting a relatively ordered few-layer rGO structure suitable for electronic percolation. Furthermore, the formation of SnO$_2$ nanoparticles *in situ* and as the graphene network is formed (implanted in the rGO layer) suggests the compensation and repair of the degradation and discontinuity of the physico-chemical and electrical properties (dielectric, conductivity, resistivity, *etc.*) caused by the defects.

3.2.4 X-ray diffraction patterns. The crystalline phases of prepared SnO$_2$/rGO nanocomposite are investigated using X-ray

diffraction (XRD) analysis. The diffraction pattern of pure SnO$_2$ in the nanocomposite was indexed to the rutile-type SnO$_2$ phase, characterized by a tetragonal structure with space group $P4_2/mnm$, as specified in JCPDS card no. 41–1445. The calculated lattice parameter values were determined to be $a = b = 4.7524$ Å, $c = 3.1961$ Å, and unit cell volume of $V = 72.1848$ Å^3, with convergence factor values of $R_p = 6.09\%$, $R_{exp} = 6.38\%$, $R_{wp} = 8.10\%$ and GOF = 1.25 (Fig. 5a), which are consistent with the literature.[70] XRD pattern of the SnO$_2$/rGO nanocomposite is presented in Fig. 5b. The absence of diffraction peaks characteristic of native cellulose aligns with previous findings and confirms the complete structural degradation of the cellulose precursor. The diffractogram exhibits distinct peaks at 2θ values of 26.7°, 33.8°, 38.0°, 51.6°, 54.8°, 57.9°, 61.8°, 65.2°, 71.2°, and 78.5°, which are indexed to the (110), (101), (200), (211), (220), (002), (310), (301), (202), and (321) crystallographic planes, respectively.[71] This peak profile is consistent with the tetragonal rutile structure of pure SnO$_2$ (JCPDS card no. 41-1445).[72,73] Notably, a diffraction peak near 11°, typical of the graphene oxide phase, was not discernible. This absence can be attributed to the effective reduction of GO to reduced graphene oxide during synthesis and potentially to a low relative mass fraction of carbon within the composite.[74] Furthermore, the lack of a sharp graphitic peak suggests that the rGO exists in a few-layer configuration, with its stacking order disrupted by the anchored SnO$_2$ nanoparticles.[75] The mean crystallite size of the SnO$_2$ particles was estimated using the Debye–Scherrer equation (eqn (1))[76] applied to the full width at half maximum (FWHM) of the most intense (110) peak, located at 26.7°.
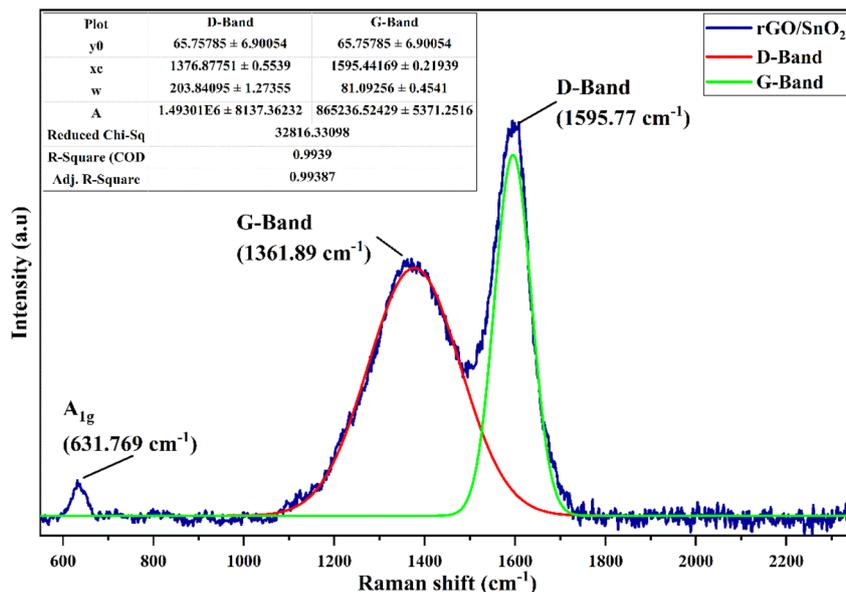
$$D = \frac{k\lambda}{\beta \cos(\theta)} \tag{1}$$

Plot	D-Band	G-Band
y0	65.75785 ± 6.90054	65.75785 ± 6.90054
xc	1376.87751 ± 0.5539	1595.44169 ± 0.21939
w	203.84095 ± 1.27355	81.09256 ± 0.4541
A	1.49301E6 ± 8137.36232	865236.52429 ± 5371.2516
Reduced Chi-Sq	32816.33098	
R-Square (COD)	0.9939	
Adj. R-Square	0.99387	

Fig. 4 Raman spectrum of the synthesized rGO/SnO$_2$ (D/G ≈ 1.72 < 3.5).
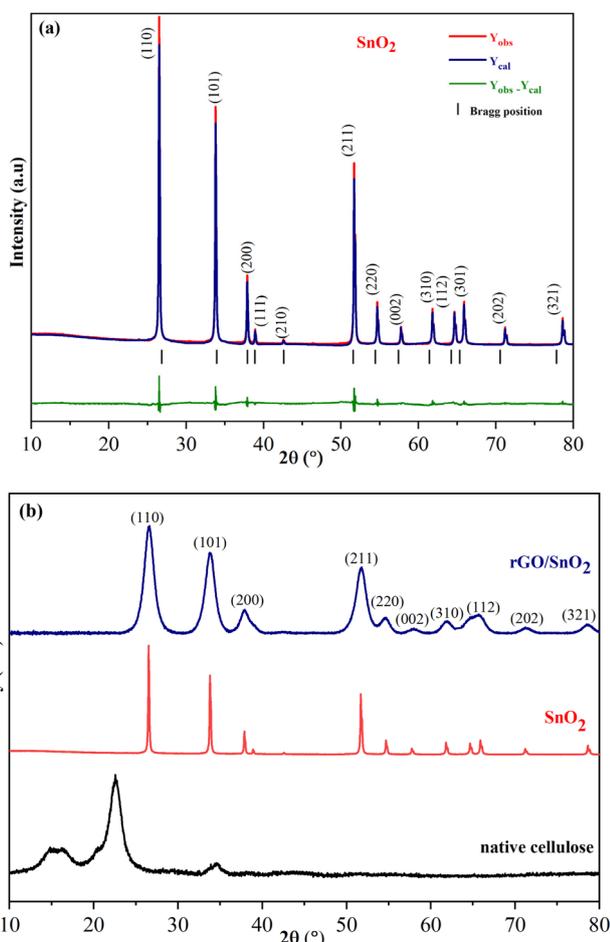
Fig. 5 (a) Rietveld analysis of SnO$_2$ and (b) X-ray diffraction patterns of native cellulose, pure SnO$_2$ and rGO/SnO$_2$ nanocomposites.

where, β is the peak width at half maximum height (FWHM) measured in radians (rad), θ denotes the Bragg diffraction angle in radians (rad), λ refers to the X-ray wavelength (1.5406 Å), and k indicates the dimensionless shape factor (0.9).

The mean crystallite size was estimated to be 43.12324 nm for pure SnO$_2$ in contrast to 5.40756 nm for the rGO/SnO$_2$ nanocomposites. Furthermore, the nanocomposites exhibit peak intensities and broader peak widths compared to pure SnO$_2$, indicating the nanoscale of the prepared nanocomposite. The broadened peaks of the composite clearly suggest a reduction in the SnO$_2$ particle size, attributable to the incorporation of rGO sheets, which also constrains the existence of SnO$_2$ precursors.[77]

3.2.5 Scanning electron microscopy (SEM) – energy dispersive X-ray (EDX) analysis. SEM imaging (Fig. 6) reveals that the microfibrous structure of native cellulose has completely disappeared, replaced by aggregated thin sheets with a flake-like morphology. This transformation confirms the complete conversion to rGO. The thickness is observed to range from a few nanometers to several tens nanometers, thereby indicating the layered structure of these materials.[78] In addition, the total disappearance of the microfibrous structure of native cellulose confirms the resulting low density of the intra and inter H-bond networks,[79] inducating the total transformation of native cellulose into rGO. Moreover, the increment in O/C ratio alongside with the presence of the tin (Sn) peak on rGO/SnO$_2$-EDX spectrum is a strong and additional findings of the success of the synthesis of rGO/SnO$_2$ from native cellulose/SnCl$_2$ system.[79] There are no isolated regions of tin agglomeration, several analyses of different grains and samples have shown the presence of Sn, validating the "one-pot" hypothesis that coordinating Sn^{2+} with cellulose prior to hydrothermal treatment ensures atomic-level mixing and uniform nucleation. The surface atomic ratios obtained *via* EDX are consistent with
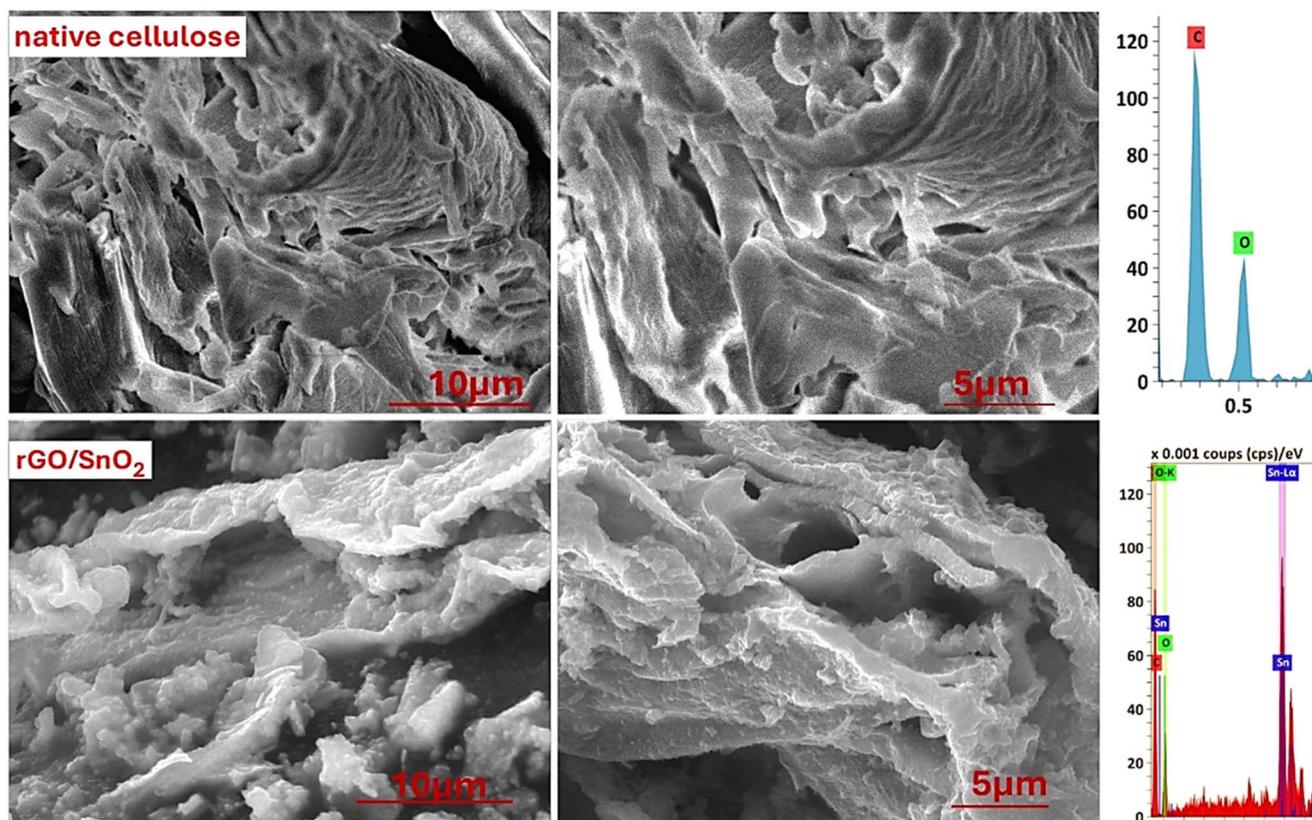
Fig. 6 SEM images and EDX spectra of native cellulose and rGO/SnO$_2$ nanocomposite.

the mass ratios calculated from TGA, confirming the compositional integrity of the composite.

3.2.6 Transmission electron microscopy (TEM). TEM analysis (Fig. 7) provides direct visual evidence of the nanostructure. Pure SnO$_2$ synthesized without cellulose exhibits spherical morphology with a diameter of 41.2 nm which is in good agreement with the value estimated from XRD diffractogram using the Scherer Debye equation. In contrast, the SnO$_2$/rGO nanocomposite displays significantly smaller SnO$_2$ nanoparticles uniformly implanted on the graphene nanosheets, with a uniform distribution of SnO$_2$ nanoparticles across the rGO surface, providing a two-dimensional distribution of implanted SnO$_2$ within the graphene sheet structure.

To statistically validate the particle size, we performed a size distribution analysis on 20 randomly selected particles from the TEM micrographs. The resulting histogram displays a narrow normal distribution with a mean particle diameter of 4.7 ± 0.5 nm. The slight deviation between TEM (4.7 nm) and XRD (5.4 nm) values is within experimental error and may arise from the Scherrer equation's volume-weighting *versus* the number-weighting of TEM counting. This value is in excellent agreement with the crystallite size calculated from XRD, confirming that the rGO sheets effectively inhibit the Ostwald ripening and growth of SnO$_2$ crystals. Furthermore, the high-resolution TEM image showed the (110) crystalline plane that recorded at different locations, where yellow parallel lines were added to

denote the interplanar distances (*d*-spacing), measured around 0.47 nm, in good agreement with the observed and refined XRD pattern of SnO$_2$.

3.3 Computational studies

3.3.1 Molecular geometry. To gain a molecular-level understanding of how graphene interacts with SnO$_2$ clusters, computational modeling was performed using a simplified SnO$_2$ model. Instead of a large experimental nanocluster, a smaller cluster containing three SnO$_2$ units "denoted Sn$_3$O$_6$" was used to reduce computational cost. This model represents the interaction between the oxide cluster and the carbon support.[80] The initial structure was derived from crystallographic data (.cif file) and multiple plausible configurations were optimized in the gas phase to obtain the ground state geometry (Fig. 8). The geometry optimizations and property simulations were conducted with Gaussian 09 (revision D.01),[81] using Density Functional Theory (DFT) and the B3LYP functional. A hybrid basis set was selected: the 6-311G** basis set for lighter atoms and the Stuttgart/Dresden (SDD) effective core potential for the heavier tin atoms.[82] This combination allowed accurate and computationally feasible modeling, considering the small cluster size and the need to handle heavy atoms appropriately. The B3LYP functional was chosen based on prior literature indicating its bandgap predictions align well with experimental data and previous gas sensor modeling.[83]
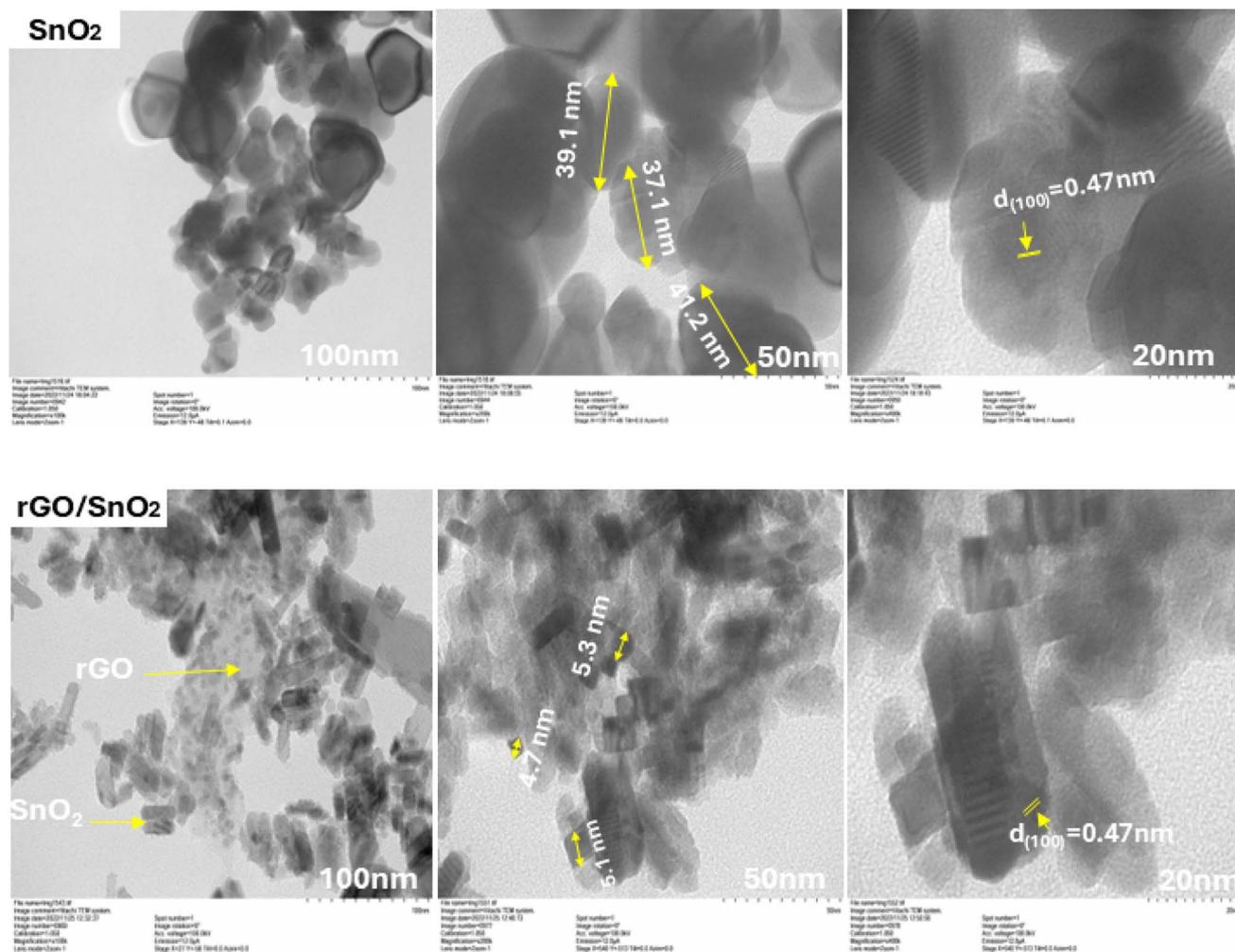
Fig. 7 TEM images of pure SnO_2 and rGO/SnO_2 nanocomposites.

Importantly, this work presents novel insights, as interactions between Sn_3O_6 clusters and reduced graphene oxide (rGO) have not been reported previously, highlighting the originality and relevance of this computational study for gas sensing material research.[84]

3.3.2 Frontier molecular orbital studies. The Frontier Molecular Orbitals (FMOs) are depicted in Fig. 9. FMOs refer to the highest occupied molecular orbital (HOMO) and the lowest unoccupied molecular orbital (LUMO) of a molecule.[85,86] These orbitals are of great significance in understanding the reactivity,
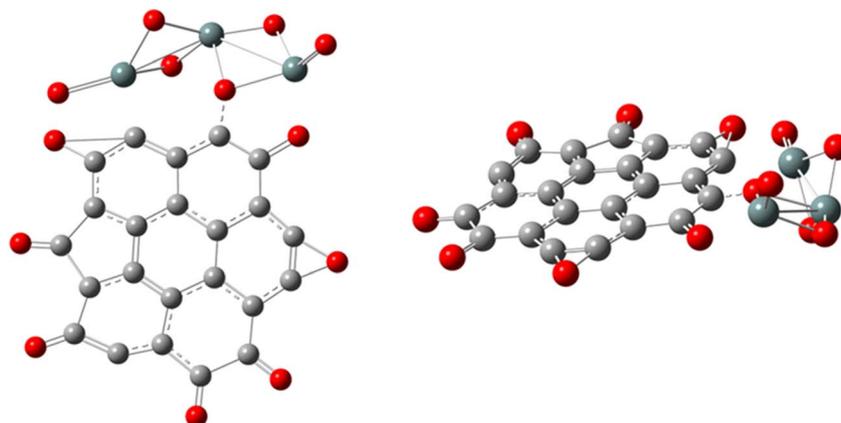
Fig. 8 The optimized molecular structures of rGO/SnO_2.
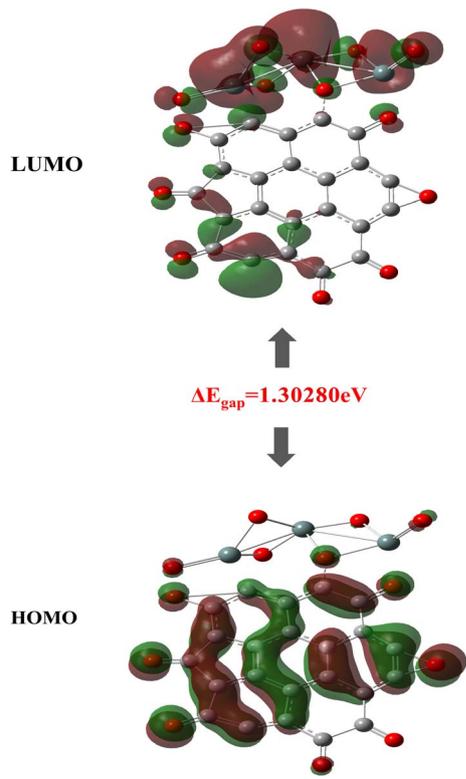
LUMO

$\Delta E_{gap} = 1.30280\,eV$

HOMO

Fig. 9 Correlation diagram between HOMO and LUMO of rGO/SnO$_2$.

stability, and electronic properties of the molecule. The HOMO represents the electron-donating ability of the molecule, while the LUMO represents the electron-accepting ability. The energy difference between the HOMO and LUMO, known as the HOMO–LUMO energy gap (ΔE_{gap}), is a critical parameter that determines the molecule's chemical reactivity and kinetic stability. The corresponding global reactivity descriptors are summarized in Table 1. The moderate calculated HOMO–LUMO9 illustrates the frontier molecular orbitals of the studied system, namely HOMO and LUMO. The corresponding global reactivity descriptors are summarized in Table 1. The moderate energy gap (ΔE_{gap}) of 1.3028 eV reflects a balanced compromise between electronic stability and chemical reactivity, which is advantageous for applications such as gas sensing and catalysis. This suggests a semiconductor nature with high chemical reactivity, advantageous for sensing applications.[84] The HOMO

Table 1 Global reactivity descriptors of rGO/SnO$_2$

Quantum chemical parameters	Values
E_{HOMO} (eV)	-6.9140
E_{LUMO} (eV)	-5.6112
ΔE_{gap} (eV)	1.3028
η (eV)	0.6514
σ (eV^{-1})	1.5352
χ (eV)	6.2626
ω (eV)	30.1045
μ (debye)	7.2551

energy level, measured at -6.9140 eV, indicates the electron-donating capability of the Sn$_3$O$_6$ cluster.[87] A relatively low HOMO energy suggests good electronic stability while maintaining sufficient ability to engage in electron transfer interactions with the reduced graphene oxide substrate. Conversely, the LUMO energy at -5.6112 eV highlights electrophilic sites that can accept electrons during molecular interactions.[88]

The global electronegativity (χ) is calculated to be 6.2626 eV, signifying a moderate tendency to attract electrons. The chemical hardness (η) value of 0.6514 eV represents a moderate resistance to changes in electron density, complemented by a softness (σ) of 1.5352 eV^{-1}, indicating a reasonable capacity for electronic polarization. These parameters collectively suggest that the Sn$_3$O$_6$ cluster possesses sufficient electronic flexibility to adapt to environmental variations, thereby facilitating effective interactions with the rGO substrate.[89] The electrophilicity index (ω), evaluated at 30.1045 eV, denotes a strong propensity to accept electron pairs, a key feature in processes involving adsorption or catalytic reactions on active surfaces. Furthermore, the relatively high dipole moment of 7.2551 debye reflects a pronounced molecular polarity, which will enhance dipole–dipole interactions and potentially orient the cluster favorably upon interaction with the rGO support.

The quantum chemical profile depicts that the Sn$_3$O$_6$ cluster supported on reduced graphene oxide as electronically stable with moderate hardness,[90] yet sufficiently reactive at specific sites, and exhibiting significant polarity. These combined features promote strong and stable interactions between the Sn$_3$O$_6$ cluster and the rGO substrate, enhancing the composite's overall structural integrity and electronic communication.[82] Such properties are crucial for optimizing the performance of Sn/rGO composites in applications like gas sensing, catalysis, and energy storage devices.

3.3.3 MEP surface analysis. The Molecular Electrostatic Potential (MEP) surface of the Sn$_3$O$_6$/rGO composite (Fig. 10) displays a predominantly homogeneous and neutral charge distribution, indicated by a dominant green coloration.[88] This uniformity reflects a balanced electronic environment across the composite surface, devoid of strongly electrophilic or nucleophilic regions. Such electronic neutrality suggests moderately charged reactive sites, which support stable and balanced interactions with diverse external species while preventing strong non-specific binding. This characteristic enables sensitive dipole–dipole interactions with target analytes.[41] The incorporation of heteroatoms, specifically oxygen and nitrogen, within the Sn$_3$O$_6$ cluster and on the rGO surface promotes a uniform charge distribution. This enhances electronic compatibility with target analyte molecules, thereby optimizing adsorption and interaction energetics.[90] Consequently, the MEP surface reveals an electrostatically balanced surface topology for the Sn$_3$O$_6$/rGO composite. This balanced charge environment is a critical determinant for fostering efficient and stable interfacial interactions with reactant species, a key factor underpinning the composite's enhanced performance in applications such as heterogeneous catalysis and chemoresistive sensing.

3.3.4 ELF – LOL analysis. The combined analysis of the Electron Localization Function (ELF) and the Localized Orbital
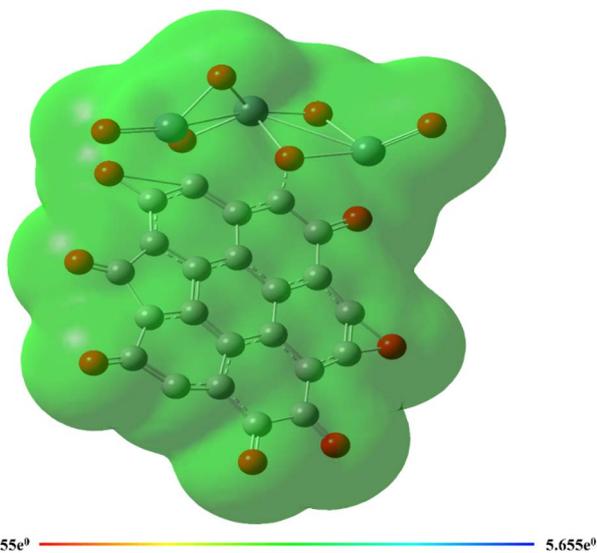
Fig. 10 MEP surface of rGO/SnO$_2$.

Locator (LOL) constitutes a robust theoretical framework for probing the nuanced interplay between electronic distribution and molecular geometry, as well as for elucidating the nature of chemical bonding at reactive sites.[91] These quantum chemical descriptors have been extensively employed in the literature to gain deeper insights into electron localization phenomena and bonding topologies across a wide array of molecular systems. As depicted in Fig. 11, the ELF map highlights regions of significant electron localization, represented by intense red isosurfaces predominantly surrounding oxygen atoms and within C–C and C–O bonding domains. These features are indicative of localized electron pairs, characteristic of covalent bonding or nonbonding lone pairs, as well as core electron shells. In contrast, certain oxygen atoms within carbonyl moieties and selected carbon centers exhibit a distinct blue coloration, reflecting regions of reduced localization associated with delocalized electron clouds.[92]

The LOL representations shown in Fig. 5 further complement this analysis. A predominance of bright white regions is observed around carbon atoms, corresponding to areas where the local electron density exceeds the upper threshold of the visualization scale, typically within the valence shell.[93] Notably, coherent blue regions appear consistently in the vicinity of tin (Sn) atoms, suggesting the presence of electron-depleted zones situated between the valence and inner core regions, indicative of reduced electron localization in these sites.[94] Collectively, the insights derived from ELF and LOL analyses offer a comprehensive depiction of the electronic structure,[95] providing critical information on bonding characteristics, electron delocalization, and the electronic environment within the investigated molecular frameworks. This dual approach significantly enhances our understanding of structure–property relationships and the reactivity of complex molecular systems.[96]

4 Conclusion

This study establishes a novel, environmentally benign single-pot hydrothermal synthesis for the direct conversion of native cellulose and tin(II) chloride into a well-defined reduced graphene oxide/tin dioxide (rGO/SnO$_2$) nanocomposite. This approach represents a significant advancement in sustainable material fabrication by utilizing a ubiquitous biomass precursor to concurrently generate the conductive rGO matrix and SnO$_2$ nanocrystals *in situ*, thereby eliminating the need for multi-step procedures involving pre-synthesized graphene derivatives or harsh chemical reductants. A comprehensive suite of characterization techniques, including ATR-FTIR, Raman spectroscopy, XRD, SEM/EDX, TEM, and TGA, confirms the formation of a composite architecture consisting of ultrasmall (~5.4 nm average diameter, as per XRD, Scherrer equation, and TEM statistics) rutile-phase SnO$_2$ nanoparticles uniformly anchored on a few-layer, low-defect rGO framework. The process leverages SnCl$_2$ dually as a catalyst for cellulose carbonization *via* a Sn-catalyzed 5-HMF pathway and as the
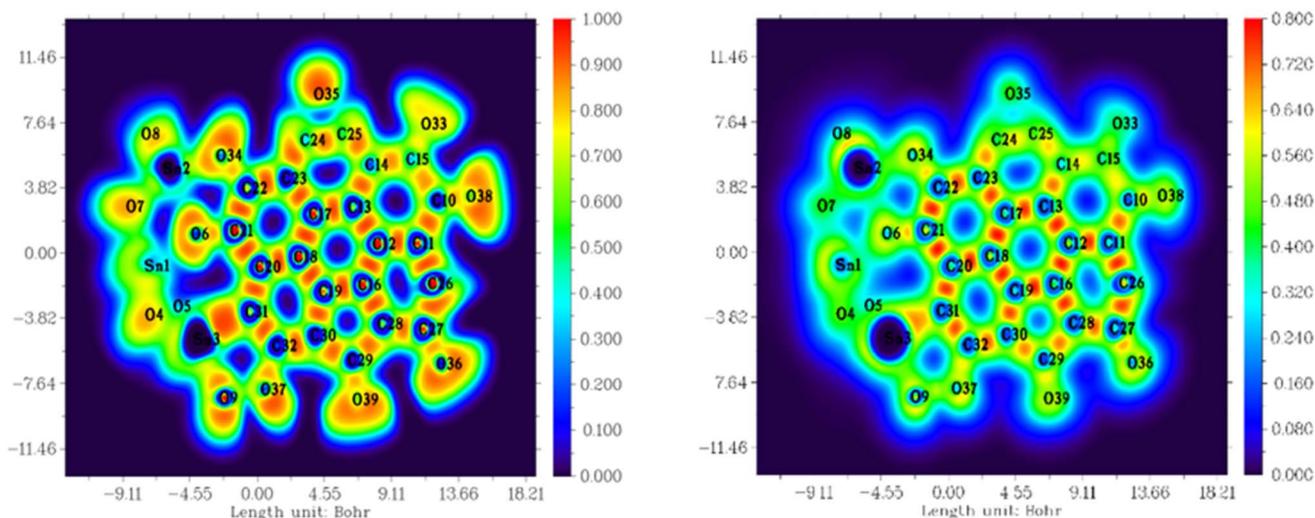

Fig. 11 Electron localization function (ELF) map and localized orbital locator (LOL) maps and contour surface of rGO/SnO$_2$.

metal oxide precursor, eliminating toxic reagents and complex exfoliation steps. Thermogravimetric and EDX analyses verify a thermally stable composite with a high carbon-to-oxide ratio, essential for establishing an extensive conductive network.

The electronic properties and interfacial coupling within the composite are elucidated through Density Functional Theory (DFT) calculations on an Sn_3O_6-rGO model system. These computations reveal a moderate band gap of 1.30 eV, significant surface electrophilicity, and an overall balanced electrostatic surface potential. This electronic structure confirms robust interfacial synergy, which promotes favorable adsorbate interactions and efficient charge–transfer processes. The resulting microstructure, characterized by quantum-confined oxide domains, intimate interfacial contact, and a percolative conductive network, embodies key design principles for high-performance functional materials.

Consequently, the cellulose-derived rGO/SnO_2 nanocomposite demonstrates direct application potential. It is highly promising for use as a high-rate alkali-ion battery anode, where the rGO matrix dually buffers volume changes and enhances electrical conductivity. Its pronounced electrophilic character suggests high efficacy in electrocatalytic reactions such as the oxygen reduction reaction (ORR) and nitrogen reduction reaction (NRR). Moreover, its extensive active surface area and optimized charge transport pave the way for high-sensitivity, room-temperature chemoresistive gas sensors. Compared to conventional reagent-intensive syntheses, this biomass-driven approach offers a compelling paradigm shift by minimizing chemical inputs and processing steps while delivering high-performance outputs, thereby aligning advanced nanomaterial design with green chemistry principles.

While this work establishes the synthesis, structure, and electronic properties, future studies will employ BET and Non-Linear Density Functional Theory (NLDFT) analyses to precisely quantify porosity and specific surface area, parameters critical for maximizing gas-sensing sensitivity. Nevertheless, the present results demonstrate that this green chemistry strategy provides a scalable, high-quality alternative to traditional hazardous synthesis routes for advanced energy and sensing materials.

While this study successfully demonstrates the synthesis, structure, and electronic properties of the nanocomposite, several avenues remain for further investigation. Future work will employ BET and Non-Linear Density Functional Theory (NLDFT) analyses to precisely quantify porosity and specific surface area, parameters critical for maximizing gas-sensing sensitivity and catalytic performance. Additionally, systematic electrochemical and electrocatalytic testing, such as half/full-cell battery evaluations, ORR polarization measurements, and gas-sensing response studies under varied atmospheres, are essential to validate the theoretical predictions and benchmark performance against existing materials. Further optimization of synthesis parameters (*e.g.*, temperature, precursor ratio, and reaction time) could fine-tune nanoparticle size, distribution, and interfacial bonding. Expanding the methodology to other biomass sources or metal precursors may also yield a broader family of sustainable nanocomposites. Ultimately, this green

synthesis strategy not only provides a scalable, high-quality alternative to conventional routes but also opens a versatile materials platform for next-generation energy storage, catalysis, and environmental sensing technologies.

Author contributions

Conflicts of interest

The authors declare no conflicts interest.

Data availability

The data supporting the findings of this study are available within the article. Additional characterization data and computational input/output files related to the DFT calculations are available from the corresponding author upon request.

Acknowledgements

References

1 D. Nayak, S. Mourya, S. Ansari, R. K. Sahoo and R. Choudhary, 2025, DOI: 10.1039/9781837673391-00080.

2 B. Chen, H. Qian, J. Xu, L. Qin, Q.-H. Wu, M. Zheng and Q. Dong, *J. Mater. Chem. A*, 2014, **2**, 9345–9352.

3 J. Sang, K. Liu, X. Zhang, S. Zhang, G. Cao, Y. Shen and G. Shao, *Energy Environ. Mater.*, 2023, **6**, e12431.

4 B. Dursun, E. Topac, R. Alibeyli, A. Ata, O. Ozturk and R. Demir-Cakan, *J. Alloys Compd.*, 2017, **728**, 1305–1314.

5 K. Chu, Y. P. Liu, Y. B. Li, J. Wang and H. Zhang, *ACS Appl. Mater. Interfaces*, 2019, **11**, 31806–31815.

6 N. Garino, A. Sacco, M. Castellino, J. A. Munoz-Tabares, A. Chiodoni, V. Agostino, V. Margaria, M. Gerosa, G. Massaglia and M. Quaglio, *ACS Appl. Mater. Interfaces*, 2016, **8**, 4633–4643.

7 Z. A. M. Alaizeri, H. A. Alhadlaq, S. Aldawood, M. J. Akhtar and M. Ahamed, *Polymers*, 2022, **14**, 2036.

8 P. Van Tuan, H. B. Tuong, V. T. Tan, L. H. Thu, N. D. Khoang and T. N. Khiem, *Opt. Mater.*, 2022, **123**, 111916.

9 F. Davar, M. Salavati-Niasari and Z. Fereshteh, *J. Alloys Compd.*, 2010, **496**, 638–643.

10 M. Salavati-Niasari, N. Mir and F. Davar, *Inorg. Chim. Acta*, 2010, **363**, 1719–1726.

11 A. Mallik, I. Roy, D. Chalapathi, C. Narayana, T. Das, A. Bhattacharya, S. Bera, S. Bhattacharya, S. De and B. Das, *J. Mater. Sci. Eng. B*, 2021, **264**, 114938.

12 D. Zhang, A. Liu, H. Chang and B. Xia, *RSC Adv.*, 2015, **5**, 3016–3022.

13 K. C. Lam, B. Huang and S. Q. Shi, *J. Mater. Chem. A*, 2017, **5**, 11131–11142.

14 K. S. Novoselov, V. I. Fal'ko, L. Colombo, P. R. Gellert, M. G. Schwab and K. Kim, *Nature*, 2012, **490**, 192–200.

15 S. Rao, J. Upadhyay, K. Polychronopoulou, R. Umer and R. Das, *J. Compos. Sci.*, 2018, **2**, 25.

16 E. Jaafar, M. Kashif, S. K. Sahari and Z. Ngaini, *Mater. Sci. Forum*, 2018, **917**, 112–116.

17 R. Bhargava, S. Khan, N. Ahmad and M. Mohsin Nizam Ansari, *Mater. Today: Proc.*, 2019, **18**, 5012–5018.

18 S. Park, J. An, J. R. Potts, A. Velamakanni, S. Murali and R. S. Ruoff, *Carbon*, 2011, **49**, 3019–3023.

19 Z.-z. Yang, Q.-b. Zheng, H.-x. Qiu, J. Li and J.-h. Yang, *N. Carbon Mater.*, 2015, **30**, 41–47.

20 S. Pei, J. Zhao, J. Du, W. Ren and H.-M. Cheng, *Carbon*, 2010, **48**, 4466–4474.

21 K. K. H. De Silva, H.-H. Huang and M. Yoshimura, *Appl. Surf. Sci.*, 2018, **447**, 338–346.

22 Z. Khosroshahi, M. Kharaziha, F. Karimzadeh and A. Allafchian, 2018.

23 Y. Liu, Y. Zhang, G. H. Ma, Z. Wang, K. Y. Liu and H. T. Liu, *Electrochim. Acta*, 2013, **88**, 519–525.

24 X.-Z. Tang, X. Li, Z. Cao, J. Yang, H. Wang, X. Pu and Z.-Z. Yu, *Carbon*, 2013, **59**, 93–99.

25 F. Mindivan and M. Göktaş, *Mater. Test.*, 2019, **61**, 1007–1011.

26 F. Liu, C. J. Wang, X. Sui, M. A. Riaz, M. Y. Xu, L. Wei and Y. Chen, *Carbon Energy*, 2019, **1**, 173–199.

27 V. Nanjundappa, T. Ramakrishnappa, H. Prakash and B. Praveen, *Appl. Surf. Sci. Adv.*, 2023, **14**, 100386.

28 M. Cai, D. Thorpe, D. H. Adamson and H. C. Schniepp, *J. Mater. Chem.*, 2012, **22**, 24992–25002.

29 Y. Chen, L. Qin, Y. Lei, X. Li, J. Dong, D. Zhai, B. Li and F. Kang, *ACS Appl. Mater. Interfaces*, 2019, **11**, 45578–45585.

30 L. Banszerus, M. Schmitz, S. Engels, J. Dauber, M. Oellers, F. Haupt, K. Watanabe, T. Taniguchi, B. Beschoten and C. Stampfer, *Sci. Adv.*, 2015, **1**, e1500222.

31 G. Li, Y. Y. Zhang, H. Guo, L. Huang, H. Lu, X. Lin, Y. L. Wang, S. Du and H. J. Gao, *Chem. Soc. Rev.*, 2018, **47**, 6073–6100.

32 Z. Lu, Z. Kong, L. Jing, T. Wang, X. Liu, A. Fu, P. Guo, Y.-G. Guo and H. Li, *Energy Fuels*, 2020, **34**, 13126–13136.

33 P. Jena, N. Naresh, N. Satyanarayana, P. K. Patro, R. Biswal and M. Adhikary, *J. Mater. Sci.: Mater. Electron.*, 2021, **32**, 7619–7629.

34 L. Zeng, M. Liu, P. Li, G. Zhou, P. Zhang and L. Qiu, *Sci. China Mater.*, 2020, **63**, 1920–1928.

35 R. Sharma, H. Kumar, D. Yadav, C. Saini, R. Kumari, G. Kumar, A. B. Kajjam, V. Pandit, M. Ayoub, Saloni, Y. Deswal and A. K. Sharma, *J. Energy Storage*, 2024, **93**, 112317.

36 M. Khan, M. N. Tahir, S. F. Adil, H. U. Khan, M. R. H. Siddiqui, A. A. Al-warthan and W. Tremel, *J. Mater. Chem. A*, 2015, **3**, 18753–18808.

37 M. H. SM, A. M. Al-Dhahebi and M. S. Mohamed Saheed, *Polymers*, 2022, **14**, 5125.

38 L. Nejati Moghadam and M. Salavati-Niasari, *J. Mol. Struct.*, 2017, **1146**, 629–634.

39 R. Monsef and M. Salavati-Niasari, *J. Mater. Sci. Eng. B*, 2024, **310**, 117743.

40 S. Zinatloo-Ajabshir, M. S. Morassaei and M. Salavati-Niasari, *J. Environ. Manage.*, 2019, **233**, 107–119.

41 O. Azougagh, S. Essayeh, N. Achalhi, A. El Idrissi, H. Amhamdi, M. Loutou, Y. El Ouardi, A. Salhi, M. Abou-Salama and S. El Barkany, *Carbohydr. Polym.*, 2022, **276**, 118737.

42 L. Jabir, H. El-Hammi, N. Mohammed, I. Jilal, A. El Idrissi, H. Amhamdi, M. Abou-Salama, Y. El Ouardi, S. El Barkany and K. Laatikainen, *Cellulose*, 2022, **29**, 4539–4564.

43 H. El-Hammi, S. E. Barkany, L. Jabir, O. Azougagh, I. Jilal, N. Achalhi, A. Salhi, A. E. Idrissi, Y. E. Ouardi, M. Abou-Salama and K. Laatikainen, 2023, DOI: 10.21203/rs.3.rs-2970659/v1.

44 N. Achalhi, Y. El Ouardi, S. Virolainen, R. El yousfi, M. Lamsayah, S. Butylina, S. El Barkany, E. Repo and A. El Idrissi, *Cellulose*, 2024, **31**, 9887–9906.

45 D. Valde, L. Dadsena, C. Kuppam, M. Mohanta, T. Maharana and S. E. Jujjavarapu, *Energy Technol.*, 2025, e202500676.

46 A. G. Nandgaonkar, Q. Wang, K. Fu, W. E. Krause, Q. Wei, R. Gorga and L. A. Lucia, *Green Chem.*, 2014, **16**, 3195–3201.

47 A. Herbst and C. Janiak, *New J. Chem.*, 2016, **40**, 7958–7967.

48 F. Jiang, Q. Zhu, D. Ma, X. Liu and X. Han, *J. Mol. Catal. A: Chem.*, 2011, **334**, 8–12.

49 S. Premkumar, K. Radhakrishnan, R. Kalidoss, J. V. Kumar, N. Abirami and B. S. Inbaraj, *Catalysts*, 2023, **13**, 381.

50 S. Premkumar, K. Radhakrishnan, R. Kalidoss, J. V. Kumar, N. Abirami and B. S. Inbaraj, *Catalysts*, 2023, **13**, 381.

51 S. Knop, T. L. C. Jansen, J. Lindner and P. Vöhringer, *Phys. Chem. Chem. Phys.*, 2011, **13**, 4641–4650.

52 W. Chen, H. He, H. Zhu, M. Cheng, Y. Li and S. Wang, *Polymers*, 2018, **10**, 592.

53 M. Arshad, A. Maaroufi, G. Pinto, S. El-Barkany and A. Elidrissi, *Bull. Mater. Sci.*, 2016, **39**, 1609–1618.

54 N. Johar, I. Ahmad and A. Dufresne, *Ind. Crops Prod.*, 2012, **37**, 93–99.

55 C. Pappas, P. Tarantilis, I. Daliani, T. Mavromoustakos and M. Polissiou, *Ultrason. Sonochem.*, 2002, **9**, 19–23.

56 S. El Barkany, A. El Idrissi, S. Ouslimane and H. Amhamdi, *Phys. Chem. News*, 2009, **46**, 135e141.

57 A. El Idrissi, S. El Barkany, H. Amhamdi and A. K. Maaroufi, *J. Appl. Polym. Sci.*, 2013, **127**, 3633–3644.

58 Q. Wang, N. Plylahan, M. V. Shelke, R. R. Devarapalli, M. Li, P. Subramanian, T. Djenizian, R. Boukherroub and S. Szunerits, *Carbon*, 2014, **68**, 175–184.

59 H. Shen, X. Zhao, L. Duan, R. Liu, H. Wu, T. Hou, X. Jiang and H. Gao, *Appl. Surf. Sci.*, 2017, **391**, 627–634.

60 M. K. Singh, R. K. Pandey and R. Prakash, *Org. Electron.*, 2017, **50**, 359–366.

61 S. B. Singh and S. A. Dastgheib, *Carbon Trends*, 2025, **20**, 100511.

62 M. Varshini and R. Manimekalai, *J. Mater. Sci. Eng. B*, 2025, **317**, 118214.

63 R. Al-Gaashani, A. Najjar, Y. Zakaria, S. Mansour and M. A. Atieh, *Ceram. Int.*, 2019, **45**, 14439–14448.

64 S. Naz, I. Javid, S. Konwar, K. Surana, P. K. Singh, M. Sahni and B. Bhattacharya, *SN Appl. Sci.*, 2020, **2**, 1–8.

65 A. Kumar, L. Rout, R. S. Dhaka, S. L. Samal and P. Dash, *RSC Adv.*, 2015, **5**, 39193–39204.

66 N. Sharma, V. Sharma, Y. Jain, M. Kumari, R. Gupta, S. Sharma and K. Sachdev, 2017.

67 R. Peng, X. Zhuang, Y. Li, Z. Yu and L. Ci, *Coatings*, 2023, **13**, 849.

68 A. C. Ferrari, J. C. Meyer, V. Scardaci, C. Casiraghi, M. Lazzeri, F. Mauri, S. Piscanec, D. Jiang, K. S. Novoselov, S. Roth and A. K. Geim, *Phys. Rev. Lett.*, 2006, **97**, 187401.

69 S. Chen, B. Zhu, T. Xing, J. Yang and Y. Gu, *Mater. Res. Express*, 2022, **9**, 106201.

70 W. B. Soltan, S. Nasri, M. S. Lassoued and S. Ammar, *J. Mater. Sci.: Mater. Electron.*, 2017, **28**, 6649–6656.

71 Q.-l. Lu, X.-y. Li, L.-r. Tang, B.-l. Lu and B. Huang, *RSC Adv.*, 2015, **5**, 56198–56204.

72 P. Van Tuan, H. B. Tuong and T. N. Khiem, *Commun. Phys.*, 2021, **31**, 361–368.

73 F. Sujatmiko, I. Sahroni, G. Fadillah and I. Fatimah, *Open Chem.*, 2021, **19**, 174–183.

74 H. Seema, K. C. Kemp, V. Chandra and K. S. Kim, *Nanotechnology*, 2012, **23**, 355705.

75 Y. Liu, Y. Jiang, Y. Lv, Z. He, L. Dai and L. Wang, *Molecules*, 2021, **26**, 5085.

76 A. Patterson, *Phys. Rev.*, 1939, **56**, 978.

77 H. Osora, D. Kolkoma, G. Anduwan, M. Waimbo and S. Velusamy, *J. Cluster Sci.*, 2024, **35**, 891–901.

78 A. Shalaby, D. Nihtianova, P. Markov, A. Staneva, R. Iordanova and Y. Dimitriev, *Bulg. Chem. Commun.*, 2015, **47**, 291–295.

79 H. El-Hammi, S. El Barkany, L. Jabir, O. Azougagh, I. Jilal, N. Achalhi, A. Salhi, A. El Idrissi, Y. El Ouardi, M. Abou-Salama and K. Laatikainen, *Cellulose*, 2024, **31**, 2079–2103.

80 J. B. L. Martins, E. Longo, J. Andrés and C. A. Taft, *J. Mol. Struct.:THEOCHEM*, 1995, **335**, 167–174.

81 Z. Wang, Y. Zhang, S. Liu and T. Zhang, *Sens. Actuators, B*, 2016, **222**, 893–903.

82 S. Zheng, Y. Li, J. Hao, H. Fang, Y. Yuan, H.-S. Tsai, Q. Sun, P. Wan, X. Zhang and Y. Wang, *Appl. Surf. Sci.*, 2021, **568**, 150926.

83 W. H. Baur and A. A. Khan, *Acta Crystallogr., Sect. B*, 1971, **27**, 2133–2139.

84 K. Khayer and T. Haque, *ACS Omega*, 2020, **5**, 4507–4531.

85 A. Frisch, A. B. Nielson and A. J. Holder, *Gaussview user manual*, Gaussian Inc., Pittsburgh, PA, 2000, p. 556.

86 T. Lu and F. Chen, *J. Comput. Chem.*, 2012, **33**, 580–592.

87 P. Geerlings and F. De Proft, *Int. J. Mol. Sci.*, 2002, **3**, 276–309.

88 O. Azougagh, I. Jilal, L. Jabir, H. El-Hammi, S. Essayeh, N. Mohammed, N. Achalhi, R. El yousfi, A. El Idrissi, Y. El Ouardi, K. Laatikainen, M. Abou-Salama and S. El Barkany, *Phys. Chem. Chem. Phys.*, 2023, **25**, 22870–22888.

89 A. Al Sheikh Ali, D. Khan, A. Naqvi, F. F. Al-blewi, N. Rezki, M. R. Aouad and M. Hagar, *ACS Omega*, 2021, **6**, 301–316.

90 P. G. Ashmore and M. G. Burnett, *Trans. Faraday Soc.*, 1962, **58**, 253–261.

91 F. Akman, A. Demirpolat, A. S. Kazachenko, A. S. Kazachenko, N. Issaoui and O. Al-Dossary, *Molecules*, 2023, **28**, 2684.

92 N. Nairat, O. Hamed, A. Berisha, S. Jodeh, M. Algarra, K. Azzaoui, O. Dagdag and S. Samhan, *BMC Chem.*, 2022, **16**, 43.

93 K.-M. Xu, S. Jiang, Y.-P. Zhu, T. Huang, Y.-R. Liu, Y. Zhang, Y.-Z. Lv and W. Huang, *RSC Adv.*, 2015, **5**, 26071–26080.

94 A. S. Kazachenko, E. Tanış, F. Akman, M. Medimagh, N. Issaoui, O. Al-Dossary, L. G. Bousiakou, A. S. Kazachenko, D. Zimonin and A. M. Skripnikov, *Molecules*, 2022, **27**, 7864.

95 K. K, D. M. J, C. T, V. P and A. R, *Struct. Chem.*, 2024, **35**, 1307–1333.

96 N. Kanagathara, V. J. Thanigaiarasu, V. Ragavendran, M. K. Marchewka, L. Saravanan and A.-Y. Lo, *Heliyon*, 2023, **9**(4), e14879.